

Ruddlesden–Popper Phases of Methylammonium-Based Two-Dimensional Perovskites with 5-Ammonium Valeric Acid $\text{AVA}_2\text{MA}_{n-1}\text{Pb}_n\text{I}_{3n+1}$ with $n = 1, 2,$ and 3

Negar Ashari-Astani,^{†,‡,§,¶} Farzaneh Jahanbakhshi,^{‡,§,¶} Marko Mladenović,^{‡,||} Anwar Q. M. Alanazi,[§] Iman Ahmadabadi,[†] Mohammad Reza Ejtehadi,[†] M. Ibrahim Dar,^{§,¶} Michael Grätzel,^{§,¶} and Ursula Rothlisberger^{*,‡,¶}

[†]Soft Condensed Matter (SCM), Sharif University of Technology, Tehran, Iran

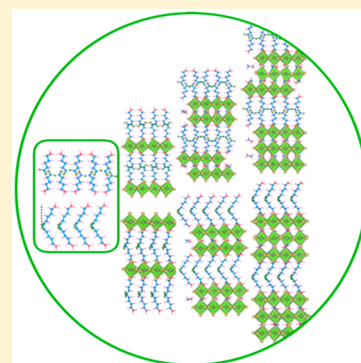
[‡]Laboratory of Computational Chemistry and Biochemistry (LCBC), École Polytechnique Fédérale de Lausanne (EPFL), CH-1015 Lausanne, Switzerland

[§]Laboratory of Photonics and Interfaces (LPI), École Polytechnique Fédérale de Lausanne (EPFL), CH-1015 Lausanne, Switzerland

^{||}Scientific Computing Laboratory, Center for the Study of Complex Systems, Institute of Physics Belgrade, University of Belgrade, Pregrevica 118, 11080 Belgrade, Serbia

S Supporting Information

ABSTRACT: 5-Ammonium valeric acid (AVA) is a frequently used additive in the preparation of lead halide perovskites. However, its microscopic role as passivating, cross-linking, or templating agent is far from clear. In this work, we provide density functional theory-based structural models for the Ruddlesden–Popper (RP) phases of $\text{AVA}_2(\text{CH}_3\text{NH}_3)_{n-1}\text{Pb}_n\text{I}_{3n+1}$ for $n = 1, 2,$ and 3 and validate with experimental data on polycrystalline samples for $n = 1$. The structural and electronic properties of the AVA-based RP phases are compared to the ones of other linker families. In contrast to aromatic and aliphatic spacers without additional functional groups, the RP phases of AVA are characterized by the formation of a regular and stable H-bonding network between the carbonyl head groups of adjacent AVA molecules in opposite layers. Because of these additional interactions, the penetration depth of the organic layer into the perovskite sheet is reduced with direct consequences for its crystalline phase. The possibility of forming strong interlinker hydrogen bonds may lead to an enhanced thermal stability.



In view of the rapidly rising photoconversion efficiencies of perovskite solar cells with current record values reaching >23%,¹ it becomes imperative to resolve some of the remaining issues concerning their long-term stability under operating conditions. One promising approach in this respect has been the use of organic additives.^{2,3} The microscopic role of these additives is not fully understood, but it has been shown that they can act as passivating surface layers or form fully periodic layered structures (so-called two-dimensional (2D) perovskites) or mixed 2D/3D constructs with enhanced stability. In few cases, it has been possible to prepare and resolve crystals of 2D perovskites showing that they can form Ruddlesden–Popper (RP)^{4–6} $\text{A}_2'\text{A}_{(n-1)}\text{M}_n\text{X}_{3n+1}$ or Dion–Jacobson (DJ)⁷ $\text{A}''\text{A}_{(n-1)}\text{M}_n\text{X}_{3n+1}$ phases where A' and A are monovalent organic cations and A'' is a divalent organic cation, M a divalent metal cation, and X a halide anion. Several RP perovskites with an organic ammonium ion $\text{A}' = \text{RNH}_3^+$ acting as a spacer between the 3D perovskite layers with $\text{A} = \text{MA}$ or FA ; $\text{M} = \text{Pb}^{2+}$ or Sn^{2+} , and X representing a halide anion have been prepared. In particular, butyl ammonium (BA),^{8,9} phenylethylammonium (PEA),^{10,11} hexylammonium (Hex),^{12,13} 4-ammonium butyric acid (ABA),¹⁴ AVA,^{15–17} anilinium (Anyl),¹⁸ benzyl ammonium,¹⁹ and a series of

polycyclic aromatic hydrocarbons²⁰ are some of the organic linkers that have been incorporated thus far. Very recently, also adamantyl-based ammonium linkers have been explored.²¹ Despite the general agreement about the beneficial effects on either efficiency^{9,11} and/or stability,²² the molecular origin of these effects is not clear yet. The space of possible linkers is huge and has only just started to be explored. Currently, hardly any structure–function relationships exist that could establish links between the chemical nature of the organic spacers and the resulting structural and electronic properties of the 2D or even 2D/3D perovskite materials. One issue that further complicates an understanding of the microscopic roles of organic linkers is the fact that in many experiments, it is not clear what type of structures are really present. Here, we focus on a systematic investigation of the properties of fully periodic RP phases with AVA as one of the most used additives to detect characteristic signatures that can help in identifying the presence of corresponding 2D RP perovskites experimentally.

Received: April 18, 2019

Accepted: June 10, 2019

Published: June 10, 2019

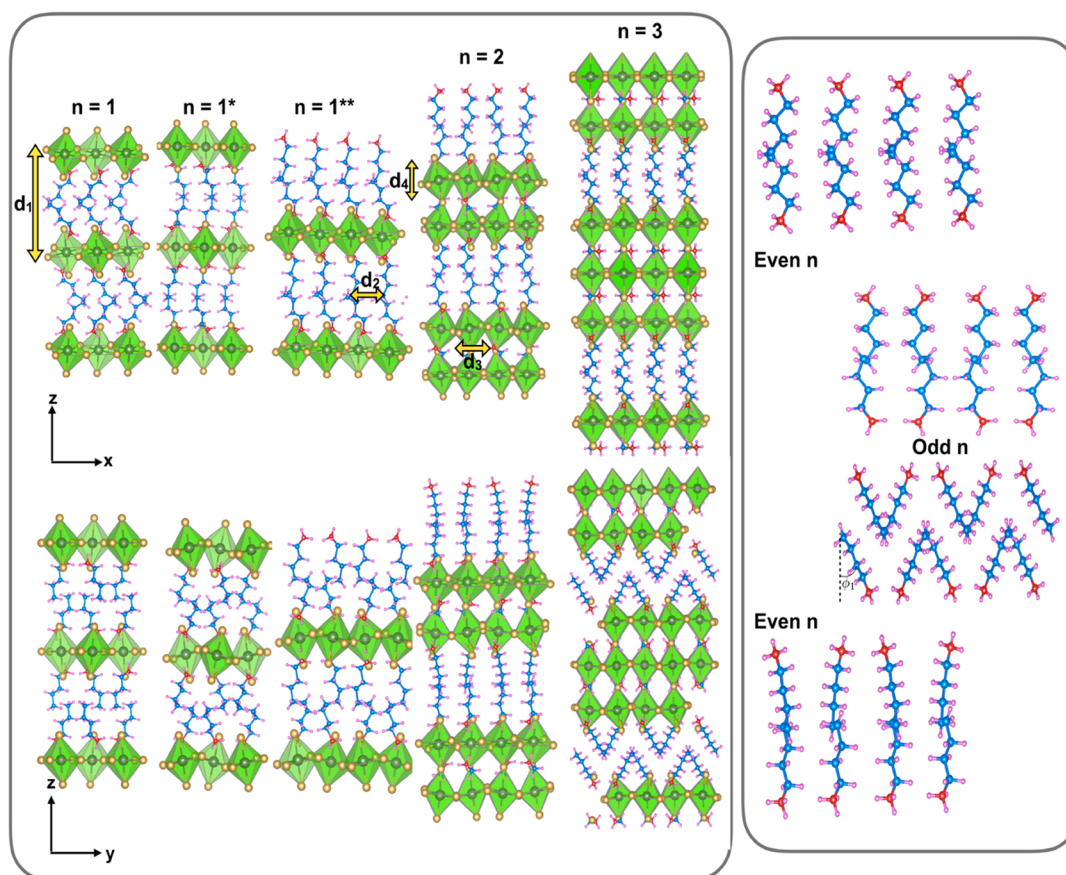


Figure 1. DFT (PBEsol)-optimized structures of $\text{BA}_2\text{MA}_{n-1}\text{Pb}_n\text{I}_{3n+1}$ for $n = 1, 2,$ and 3 viewed along the x and y axes.

Table 1. Characteristic Structural Features of $\text{BA}_2\text{MA}_{n-1}\text{Pb}_n\text{I}_{3n+1}$ for $n = 1, 2,$ and 3 Defined in the Text and in Figure 1^a

n	d_1 (Å)	d_2 (Å)	d_3 (Å)	d_4 (Å)	ϕ_1 (deg)	Θ_1 (deg), Θ_2 (deg), Θ_3 (deg)	NH..I (Å)	N..Pb (Å)
1	13.2	4.5	6.4	6.3	47	–, 113.9, 113.9	3.61	2.5
	13.1	4.5	6.4	6.3	48	–, 111.1, 111.1	3.69	2.6
1*	14.0	4.3	6.3	6.4	16	–, 120.0, 120.0	3.63	2.6
	13.8	4.3	6.3	6.4	17	–, 114.5, 114.5	3.71	2.6
1**	14.7	4.3	6.3	6.4	24	–, 118.4, 118.4	3.70	2.7
2	14.2	4.4	6.3	6.4	9	$86.4 \pm 4.3, 102.2 \pm 15.1, 104.1 \pm 14.1$	3.75	2.2
	13.2	4.4	6.3	6.3	11	$89.9 \pm 16.0, 90.0 \pm 0.0, 90.0 \pm 0.0$	3.97	2.2
3	12.7	4.5	6.3	6.3	38	$89.9 \pm 1.2, 96.3 \pm 4.8, 95.9 \pm 4.7$	3.86	2.1
	13.1	4.5	6.3	6.4	40	$90.1 \pm 9.9, 90.0 \pm 1.1, 90.0 \pm 1.1$	3.92	2.1
∞	–	–	6.3	6.4	–	$93.4 \pm 2.7, 117.4 \pm 1.3, 116.6 \pm 2.1$	–	–
	–	–	6.3	6.3	–	$91.7 \pm 0.0, 110.1 \pm 0.0, 110.1 \pm 0.0$	–	–

^aValues are averages over all corresponding distances, angles, and bonds with experimental values given in *italics*.

To this end, we use density functional theory (DFT)-based static calculations as well as molecular dynamics (MD) simulations. In particular, we predict structural models for $n = 1, 2,$ and 3 and validate them with experimental data from X-ray powder diffraction (XRD). The structural and electronic properties of the AVA-based RP phases are compared to the ones of the BA family. Because AVA and BA differ only by the presence/absence of a carboxylic end group, such a comparison can be helpful in trying to establish the direct impact of H-bonding functionalities.

RP Phases of Butylammonium-methylammonium Lead Iodide. We first tested the accuracy of our computational approach for a system where single-crystal data on RP phases is available. In the case of $\text{BA}_2\text{MA}_{n-1}\text{Pb}_n\text{I}_{3n+1}$, crystal structures have been

resolved for $n = 1, 2,$ and 3 .^{23,24} For $n = 1$, two different structures have been determined (“1” and “1*”). As a test, we also generated an RP structure for $n = 1$ taking the $n = 2$ and $n = 3$ structures as the initial template (“1**”). The DFT-optimized systems are shown in Figure 1 (full atomic coordinates and crystal lattice parameters are given in the Supporting Information) and are compared in Table 1 with the corresponding experimental data. To trace the structural changes as a function of n and compare them to the ones of the full 3D perovskite structure of MAPbI_3 in the tetragonal room-temperature phase, we define a number of characteristic quantities (indicated in Figure 1). The properties of the organic layer will be characterized by d_1 that measures its thickness, d_2 that indicates the interspacer distance, and the

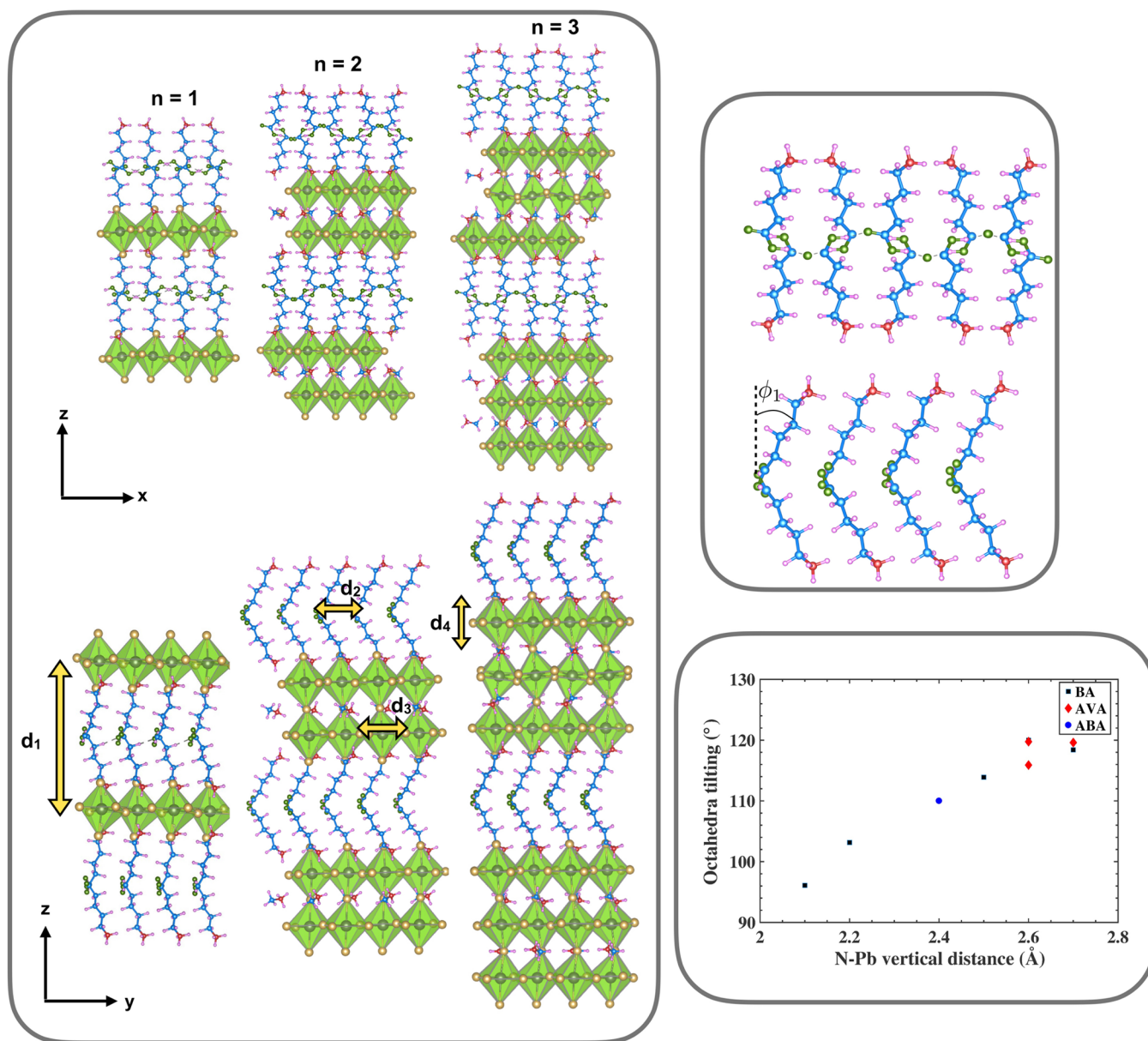


Figure 2. DFT (PBEsol)-optimized structures for $AVA_2 MA_{n-1}Pb_nI_{3n+1}$, for $n = 1, 2,$ and 3 viewed along the x and y axes. Correlation between penetration depth of the spacers (into the inorganic layer) and octahedral tilting is demonstrated in the lower-right inset.

tilting angle ϕ_1 formed by the axis defined by the average position of the carbon atoms of the organic spacer and the tetragonal axis (z). In addition, we monitor the length of the hydrogen bonds between the hydrogen atoms of the ammonium group and the neighboring iodide ions of the perovskite layer, $NH\dots I$. The inorganic perovskite part, on the other hand, will be characterized by the parameters d_3 and d_4 (defined as the distance between iodide ions in opposing octahedra corners in the xy plane and along the tetragonal axis, respectively) as well as the angles Θ_1 – Θ_3 between adjacent PbI_6^{4-} octahedra along the three crystallographic directions that characterize the distortions with respect to a cubic lattice ($\Theta_1 = \Theta_2 = \Theta_3 = 90^\circ$). Table 1 shows that the PBEsol-optimized structures are in overall good agreement with the available experimental data. The computationally generated structure (1^{**}) for $n = 1$ deduced from $n = 2$ and $n = 3$ shows properties similar to the ones of the crystal structure (1^*). As a function of n , the experimental thickness of the spacer layer is

gradually decreasing from 13.8 \AA for $n = 1^*$ to 13.1 \AA for $n = 3$; this trend is even more pronounced in the fully optimized 0 K structures where the organic layer changes from 14 to 15 \AA at $n = 1$ to 12.7 \AA at $n = 3$. Surprisingly, the tilting angle is subject to a pronounced even–odd effect (Figure 1). While $n = 3$ shows a distinct tilting, the structure for $n = 2$ is characterized by an almost perpendicular orientation of the organic chains with respect to the perovskite layer, and for $n = 1$, both structures, one with a smaller tilt around 20° and one with a large tilt of ca. 50° , exist. The rotational angle between neighboring octahedra, on the other hand, starts out with values close to the tetragonal 3D structure of MAPI with rotational angles perpendicular to the tetragonal axis around 110 – 120° but reaches values resembling a fully cubic structure for $n = 2$ and 3 . Surprisingly, the presence of the organic layer seems to stabilize a higher-symmetry perovskite structure. The electronic structure as a function of n shows the typical trend expected from a simple particle in a box model with a constant

Table 2. Characteristic Structural Features of $\text{AVA}_2\text{MA}_{n-1}\text{PbI}_{3n+1}$ for $n = 1, 2,$ and 3 Defined in the Text^a

n	d_1 (Å)	d_2 (Å)	d_3 (Å)	d_4 (Å)	ϕ_1 (deg)	Θ_1 (deg), Θ_2 (deg), Θ_3 (deg)	NH...I (Å)	N..Pb (Å)	H..O (Å)
1	17.5	4.4	6.4	6.4	16	$-119.6 \pm 3.9, 119.6 \pm 3.9$	3.90	2.7	1.5
2	16.7	4.5	6.4	6.4	30	$94.4 \pm 2.2, 119.8 \pm 1.0, 119.7 \pm 1.1$	3.68	2.6	1.6
3	17.1	4.4	6.4	6.4	27	$92.9 \pm 8.9, 115.6 \pm 11.3, 116.2 \pm 10.2$	3.63	2.6	1.6
∞	–	–	6.3	6.4	–	$93.4 \pm 2.7, 117.4 \pm 1.3, 116.6 \pm 2.1$	–	–	–
			6.3	6.3		$91.7 \pm 0.0, 110.1 \pm 0.0, 110.1 \pm 0.0$			

^aValues are averages over all corresponding distances, angles and bonds with experimental values given in *italics*.

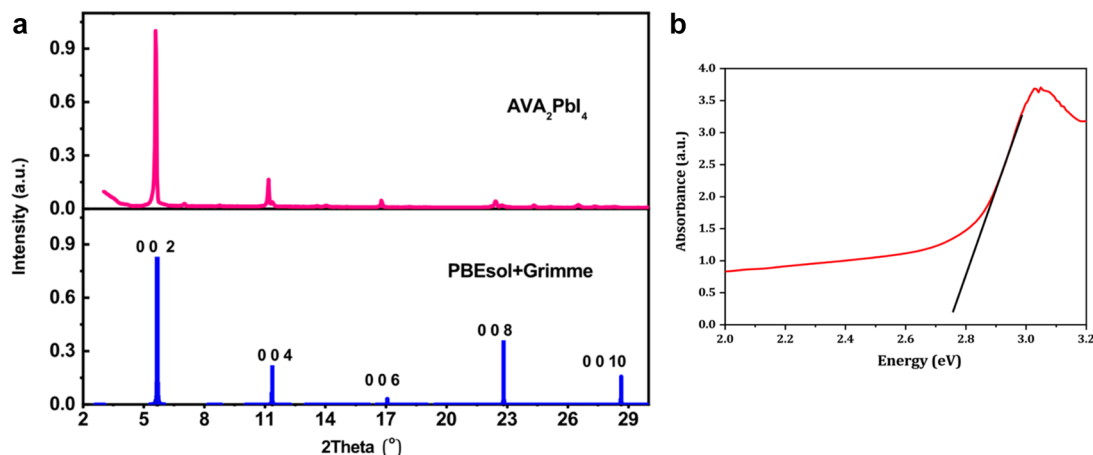


Figure 3. (a) XRD pattern of the experimental (upper panel) versus computationally (PBEsol+Grimme lower panel) predicted structure for $n = 1$. (b) Absorption spectrum and corresponding measured band gap of AVA_2PbI_4 .

decrease of the calculated band gap from 2.8 eV (for 1 and 1**) and 2.61 eV (for 1*), 2.17 eV for $n = 2$, to 1.93 eV for $n = 3$ compared to experimental values of 2.43,²³ 2.17,²³ and 2.03 eV²³ for $n = 1, 2,$ and 3 , respectively.

RP Phases of AVA-methylammonium Lead Iodide. Figure 2 shows the DFT-optimized structures of $\text{AVA}_2(\text{MA})_{(n-1)}\text{PbI}_{3n+1}$ RP perovskites for $n = 1, 2,$ and 3 , and Table 2 summarizes characteristic structural features (full atomic coordinates and crystal lattice parameters are given in the Supporting Information).

To trace the structural changes as a function of n and compare them to the ones of the full 3D perovskite structure of MAPI in the tetragonal room-temperature phase, we are using the same characteristic quantities as in the case of BA (indicated in Figure 1). In addition, we also monitor the length of the interspacer hydrogen bonds (between the O..H atoms of adjacent H-bonded AVA molecules of opposite layers). As expected because of the increased molecular length, the thickness of the spacer layer is larger than in the corresponding BA-based RP phases and decreases from 17.5 Å for $n = 1$ to 17.1 Å for $n = 3$. The compression is mainly caused by an increase in tilting of the organic chains from 16° to 27–30°. These more continuous trends are in contrast to the pronounced even/odd alteration found in the case of BA. In addition, in contrast to the RP phases of BA, the perovskite layer keeps its tetragonal structure with a gradual diminution of tetragonal distortion as indicated by the average angle between octahedra in the xy plane that decreases from 120° to 116° at $n = 3$, similar to the one observed for tetragonal 3D MAPI of 117°. Thus, while BA spacers seem to have a distinct templating effect forcing the structure of the perovskite layer into a more cubic phase away from the tetragonal room-temperature structure of MAPI, this effect seems entirely absent in the case of AVA. This is somewhat surprising,

because the AVA spacers possess an additional functional group to form strong intermolecular interactions. In search of the origin of this effect, we examined possible correlations between the octahedral tilting in the xy plane and the penetration depths of the organic layer (defined indirectly by the distance between the ammonium nitrogen atom and the nearest PbI_4 plane, reported as N..Pb in Tables 1 and 2 for the RP phases of BA and AVA, respectively). As demonstrated in the lower-right inset of Figure 2, a strong correlation is observed between increased penetration depth and a more cubic-like inorganic framework that can be rationalized by the higher spatial demand of deeply penetrating ammonium groups and the maximum of the interoctahedral space reached for a perfectly cubic structure. It is notable that in the case of BA, the absence of interlinker H-bonds allows for a deeper penetration of the spacers into the inorganic layer, which results in a more cubic framework. In the case of AVA, all three structures from $n = 1$ –3 show a regular network of H-bonds between the carboxylic groups of oppositely oriented AVA molecules (inset Figure 2) and the penetration depth is significantly lower (indicated by an increased N..Pb distance), preserving a tetragonal structure. Each AVA monomer interacts with two other spacer molecules and the H..O bond length experiences a subtle increase from 1.5 Å ($n = 1$) to 1.6 Å ($n = 3$) but indicates a strong acidic hydrogen bond in all cases. Indeed, DFT-based MD simulations at room temperature also indicate that the hydrogen-bond network is well preserved (at least on the 8 ps time scale of the simulations). This strong hydrogen-bond network clearly enhances the cohesion between the two organic layers, increasing thermal stability with respect to the case of BA.

To validate the computationally predicted structural models of the 2D perovskites of AVA, the RP phase for $n = 1$ was prepared experimentally and structurally characterized via X-

ray powder diffraction (XRD). Figure 3a shows the calculated and the experimental XRD pattern for AVA_2PbI_4 . The measured spectrum is in excellent agreement with the computationally predicted structure. The peak at $2\Theta = 5.67^\circ$ corresponds to the 002 reflection and is a measure of the thickness of the organic layer (15.6 Å) defined by the distance of Pb layers, and the corresponding experimental value (15.8 Å) corresponds to the measured low-angle peak of $2\Theta = 5.81^\circ$.

A similar comparison is not possible for the case of $n = 2$ and 3 because in this case only samples containing coexisting RP phases of $n = 2$, $n = 3$, and the 3D phase could be prepared in spite of intense efforts to synthesize pure RP phases. The measured XRD pattern as well as absorption and photoluminescence data corresponding to these mixed samples are dominated by their 3D component (Figures S4–S6) and cannot be used as a validation for the theoretically predicted RP structures. However, the superb agreement for $n = 1$ provides confidence that the computational models for $n = 2$ and 3 are equally realistic. Furthermore, the calculated band gap of 2.75 eV for AVA_2PbI_4 is also in excellent agreement with the experimentally determined value of 2.75 eV (Figure 3b), while the predicted values for $n = 2$ and $n = 3$ are 2.36 and 1.99 eV, respectively, overall similar to the ones observed for BA.²³ Full details on electronic and transport properties are given in the Supporting Information.

In summary, on the basis of DFT calculations, we predict the structure of Ruddlesden–Popper perovskites $\text{AVA}_2\text{MA}_{n-1}\text{Pb}_n\text{I}_{3n+1}$ with the frequently used additive 5-ammonium valeric acid for $n = 1, 2$, and 3 and validate the computational prediction with experimental powder diffraction and absorption data for $n = 1$. In contrast to the corresponding RP phases with butylammonium, no even/odd effects and no pronounced templating of the inorganic layer is observed. We demonstrate that there is a direct correlation between the penetration depth of the organic layer and the extent of tetragonal distortion of the perovskite layer; linkers with deep penetration drive structural transitions to more cubic frameworks. In spite of the rather different chemical nature of BA and AVA spacers and the differences in the structures of the RP phases, the overall electronic properties in terms of band gaps and effective masses are similar. However, the strong and persistent interspacer H-bond network may lend additional structural stability to AVA-based RP phases at finite temperatures.

COMPUTATIONAL METHODS

For the RP phases of AVA, the inorganic frameworks of the initial structures were constructed from the crystal structures of $(\text{BA})_2(\text{CH}_3\text{NH}_3)_{(n-1)}\text{Pb}_n\text{I}_{3n+1}$ ²³ while the initial spacer pattern was inspired by the $n = 2$ member of the 2D RP ABA family.¹⁴ DFT calculations were carried out using the Quantum Espresso suite of codes.²⁵ Structural optimizations were performed with the Perdew–Burke–Ernzerhof (PBE)²⁶ formulation revised for solids (PBEsol).²⁷ Dispersion interactions were taken into account with the empirical D3 dispersion correction.²⁸ Band gaps were calculated with PBE²⁹ and spin–orbit coupling (SOC),³⁰ which yields values in good agreement with GW.³¹ We used ultrasoft pseudopotentials to describe the interaction between valence electrons and ionic cores. Kohn–Sham orbitals were expanded in a plane wave basis set with a kinetic energy cutoff of 40 Ry and a cutoff of 280 Ry for the density. The Brillouin zone was sampled with different grids of $4 \times 1 \times 4$ and $5 \times 1 \times 5$ for $n = 1, 2$, and 3

tetragonal structures, respectively. These values were chosen by checking the convergence of total energy, band gaps, and atomic forces. Finite temperature simulations were performed for $n = 3$ using Born–Oppenheimer MD. The system was first equilibrated at room temperature and heated to higher temperatures. The temperature was controlled using the velocity rescaling implemented in Quantum Espresso.²⁵ Computational XRD patterns and reflection data of our DFT-optimized crystal structures are generated using Mercury package.³² More details on the computational setup may be found in the Supporting Information.

EXPERIMENTAL METHODS

Materials. All materials were used as received: lead iodide (PbI_2) (>98% purity, Alfa Aesar), methylammonium iodide (MAI) (>99% purity, Dyesol), 5-ammoniumvaleric acid hydroiodide (AVAI) (>99% purity, Dyesol), dimethylformamide (anhydrous, Across), and dimethyl sulfoxide (anhydrous, Across).

Perovskite Film Preparation. One molar (M) AVA_2PbI_4 precursor solution is prepared by dissolving PbI_2 and AVAI in a 1:2 molar ratio in a dimethylformamide (DMF) and dimethyl sulfoxide (DMSO) (4:1 v/v) solvent mixture. Similarly, MAI and PbI_2 (1:1 molar ratio) were dissolved in a DMF and DMSO (4:1 v/v) solvent mixture to prepare 1 M MAPbI_3 precursor solution. The AVA_2PbI_4 and MAPbI_3 were mixed in different ratios to prepare $\text{AVA}_2\text{MA}_{n-1}\text{Pb}_n\text{I}_{3n+1}$ ($n = 1, 2, \dots$) precursor solutions. Prior to mixing, both AVA_2PbI_4 and MAPbI_3 precursor solutions were heated at 65°C for 30 min. Finally, MAPbI_3 and $\text{AVA}_2\text{MA}_{n-1}\text{Pb}_n\text{I}_{3n+1}$ perovskite films were obtained by spin coating 50 μL of precursor solution on the precleaned glass substrates at 3000 rpm. The resulting films were annealed at 100°C for 30 min. The perovskite precursor solutions were prepared inside an argon glovebox, whereas perovskite film deposition was carried out inside a dry air (humidity <2%) glovebox.

Structural and Absorption Studies. X-ray diffraction (XRD) data were collected on a Philips X-ray diffractometer with a graphite monochromator, using $\text{Cu K}\alpha$ radiation. The absorption spectra of perovskite films were recorded with a UV–vis–NIR spectrophotometer (CARY-5) in transmission mode.

ASSOCIATED CONTENT

Supporting Information

The Supporting Information is available free of charge on the ACS Publications website at DOI: 10.1021/acs.jpcl.9b01111.

Characteristic structural features, crystal structure parameters, and atomic coordinates of $\text{BA}_2\text{MA}_{n-1}\text{Pb}_n\text{I}_{3n+1}$ and $\text{AVA}_2\text{MA}_{n-1}\text{Pb}_n\text{I}_{3n+1}$ for $n = 1, 2$, and 3 for PBEsol and PBEsol+Grimme optimized structures; frontier molecular orbitals and band structures of $\text{AVA}_2\text{MA}_{n-1}\text{Pb}_n\text{I}_{3n+1}$ for $n = 1, 2$, and 3; effective masses for $\text{BA}_2\text{MA}_{n-1}\text{Pb}_n\text{I}_{3n+1}$ and $\text{AVA}_2\text{MA}_{n-1}\text{Pb}_n\text{I}_{3n+1}$; XRD pattern of AVA_2PbI_4 with logarithmic scale; experimental XRD pattern and absorption and photoluminescence spectra of $\text{AVA}_2\text{MA}_{n-1}\text{Pb}_n\text{I}_{3n+1}$ for $n = 2$ and $n = 3$ (mixed samples) (PDF)

AUTHOR INFORMATION

Corresponding Author

*E-mail: ursula.roethlisberger@epfl.ch.

ORCID

Farzaneh Jahanbakhshi: 0000-0001-7113-2746

M. Ibrahim Dar: 0000-0001-9489-8365

Michael Grätzel: 0000-0002-0068-0195

Ursula Rothlisberger: 0000-0002-1704-8591

Author Contributions

#N.A.-A. and F.J. contributed equally.

Notes

The authors declare no competing financial interest.

ACKNOWLEDGMENTS

N.A.-A., M.R.E., and U.R. thank CODEV for two consecutive Seed Money grants. N.A.-A. thanks Iran nanotechnology innovation council (INIC) for funding. U.R. acknowledges Swiss NSF Grant No. 200020-165863, NCCR-MUST, NRP70, and the SINERGIA interdisciplinary research program EPISODE for funding. The authors thank the DIT/EPFL and the CSCS for the computer time. M.G. thanks the King Abdulaziz City for Science and Technology (KACST) for financial support. A.Q.M.A. gratefully acknowledges King Abdulaziz City for Science and Technology (KACST) for the fellowship.

REFERENCES

- Jeon, N. J.; Na, H.; Jung, E. H.; Yang, T. -y.; Lee, Y. G.; Kim, G.; Shin, H. -w.; Seok, S. I.; Lee, J.; Seo, J. A Fluorene-Terminated Hole-Transporting Material for Highly Efficient and Stable Perovskite Solar Cells. *Nat. Energy* **2018**, *3*, 682.
- Leijtens, T.; Eperon, G. E.; Pathak, S.; Abate, A.; Lee, M. M.; Snaith, H. J. Overcoming Ultraviolet Light Instability of Sensitized TiO₂ with Meso-Superstructured Organometal Tri-Halide Perovskite Solar Cells. *Nat. Commun.* **2013**, *4*, 2885–2885.
- Han, Y.; Meyer, S.; Dkhissi, Y.; Weber, K.; Pringle, J. M.; Bach, U.; Spiccia, L.; Cheng, Y. -b. Degradation Observations of Encapsulated Planar CH₃NH₃PbI₃ Perovskite Solar Cells at High Temperatures and Humidity. *J. Mater. Chem. A* **2015**, *3*, 8139–8147.
- Ruddlesden, S. N.; Popper, P. New Compounds of the K₂NiF₄ Type. *Acta Crystallogr.* **1957**, *10*, 538–539.
- Ruddlesden, S. N.; Popper, P. The Compound Sr₃Ti₂O₇ and Its Structure. *Acta Crystallogr.* **1958**, *11*, 54–55.
- Wang, Z.; Shi, Z.; Li, T.; Chen, Y.; Huang, W. Stability of Perovskite Solar Cells: A Prospective on the Substitution of the A Cation and X Anion. *Angew. Chem., Int. Ed.* **2017**, *56*, 1190–1212.
- Mao, L.; Ke, W.; Pedesseau, L.; Wu, Y.; Katan, C.; Even, J.; Wasielewski, M. R.; Stoumpos, C. C.; Kanatzidis, M. G. Hybrid Dion–Jacobson 2D Lead Iodide Perovskites. *J. Am. Chem. Soc.* **2018**, *140* (10), 3775–3783.
- Cao, D. H.; Stoumpos, C. C.; Farha, O. K.; Hupp, J. T.; Kanatzidis, M. G. 2d. Homologous Perovskites as Light-Absorbing Materials for Solar Cell Applications. *J. Am. Chem. Soc.* **2015**, *137*, 7843–7850.
- Zhang, X.; Ren, X.; Liu, B.; Munir, R.; Zhu, X.; Yang, D.; Li, J.; Liu, Y.; Smilgies, D.-m.; Li, R. Stable High Efficiency Two-Dimensional Perovskite Solar Cells via Cesium Doping. *Energy Environ. Sci.* **2017**, *10*, 2095–2102.
- Smith, I. C.; Hoke, E. T.; Solis-Ibarra, D.; McGehee, M. D.; Karunadasa, H. I. A Layered Hybrid Perovskite Solar-Cell Absorber with Enhanced Moisture Stability. *Angew. Chem.* **2014**, *126*, 11414–11417.
- Zhang, X.; Wu, G.; Fu, W.; Qin, M.; Yang, W.; Yan, J.; Zhang, Z.; Lu, X.; Chen, H. Orientation Regulation of Phenylethylammonium Cation Based. *Adv. Energy Mater.* **2018**, *8*, 1702498.

(12) Tanaka, K.; Kondo, T. Bandgap and Exciton Binding Energies in Lead-Iodide-Based Natural Quantum-Well Crystals. *Sci. Technol. Adv. Mater.* **2003**, *4*, 599–604.

(13) Ishihara, T.; Takahashi, J.; Goto, T. Optical Properties Due to Electronic Transitions in Two-Dimensional Semiconductors (C_nH_{2n+1}NH₃)₂PbI₄. *Phys. Rev. B: Condens. Matter Mater. Phys.* **1990**, *42*, 11099–11099.

(14) Mercier, N. (HO₂C(CH₂)₃NH₃)₂(CH₃NH₃) Pb₂I₇: A Predicted Noncentrosymmetrical Structure Built up from Carboxylic Acid Supramolecular Synthons and Bilayer Perovskite Sheets. *CrystEngComm* **2005**, *7*, 429–432.

(15) Mei, A.; Li, X.; Liu, L.; Ku, Z.; Liu, T.; Rong, Y.; Xu, M.; Hu, M.; Chen, J.; Yang, Y.; et al. A Hole-Conductor-Free, Fully Printable Mesoscopic Perovskite Solar Cell with High Stability. *Science* **2014**, *345*, 295–298.

(16) Hoshi, H.; Shigeeda, N.; Dai, T. Improved Oxidation Stability of Tin Iodide Cubic Perovskite Treated by 5-Ammonium Valeric Acid Iodide. *Mater. Lett.* **2016**, *183*, 391–393.

(17) Grancini, G.; Roldán-Carmona, C.; Zimmermann, I.; Mosconi, E.; Lee, X.; Martineau, D.; Narbey, S.; Oswald, F.; De Angelis, F.; Graetzel, M.; et al. One-Year Stable Perovskite Solar Cells. *Nat. Commun.* **2017**, *8*, 15684–15684.

(18) Rodríguez-Romero, J.; Hames, B. C.; Mora-Sero, I.; Barea, E. M. Conjugated Organic Cations to Improve the Optoelectronic Properties of 2D/3D Perovskites. *ACS Energy Letters* **2017**, *2*, 1969–1970.

(19) Iagher, L.; Etgar, L. The Effect of Cs on the Stability and Photovoltaic Performance of 2D/3D Perovskite-Based Solar Cells. *ACS Energy Letters* **2018**, *3*, 366.

(20) Passarelli, J. V.; Fairfield, D. J.; Sather, N. A.; Hendricks, M. P.; Sai, H.; Stern, C. L.; Stupp, S. I. Enhanced Out-of-Plane Conductivity and Photovoltaic Performance in *n* = 1 Layered Perovskites through Organic Cation Design. *J. Am. Chem. Soc.* **2018**, *140*, 7313–7323.

(21) Li, Y.; Milić, J. V.; Ummadisingu, A.; Seo, J.-Y.; Im, J.-H.; Kim, H.-S.; Liu, Y.; Dar, M. I.; Zakeeruddin, S. M.; Wang, P.; et al. Bifunctional Organic Spacers for Formamidinium-Based Hybrid Dion–Jacobson Two-Dimensional Perovskite Solar Cells. *Nano Lett.* **2019**, *19* (1), 150–157.

(22) Chen, Y.; Sun, Y.; Peng, J.; Tang, J.; Zheng, K.; Liang, Z. 2d. Ruddlesden–Popper Perovskites for Optoelectronics. *Adv. Mater.* **2018**, *30*, 1703487.

(23) Stoumpos, C. C.; Cao, D. H.; Clark, D. J.; Young, J.; Rondinelli, J. M.; Jang, J. I.; Hupp, J. T.; Kanatzidis, M. G. Ruddlesden–Popper Hybrid Lead Iodide Perovskite 2D Homologous Semiconductors. *Chem. Mater.* **2016**, *28*, 2852–2867.

(24) Billing, D. G.; Lemmerer, A. Synthesis, Characterization and Phase Transitions in the Inorganic–Organic Layered Perovskite-Type Hybrids [(C_nH_{2n+1}NH₃)₂PbI₄], *n* = 4, 5 and 6. *Acta Crystallogr., Sect. B: Struct. Sci.* **2007**, *63* (5), 735–747.

(25) Giannozzi, P.; Baroni, S.; Bonini, N.; Calandra, M.; Car, R.; Cavazzoni, C.; Ceresoli, D.; Chiarotti, G. L.; Cococcioni, M.; Dabo, I.; et al. A Modular and Open-Source Software Project for Quantum Simulations of Materials. *J. Phys.: Condens. Matter* **2009**, *21*, 395502.

(26) Perdew, J. P.; Burke, K.; Wang, Y. Generalized Gradient Approximation for the Exchange-Correlation Hole of a Many-Electron System. *Phys. Rev. B: Condens. Matter Mater. Phys.* **1996**, *54*, 16533–16533.

(27) Perdew, J. P.; Ruzsinszky, A.; Csonka, G. I.; Vydrov, O. A.; Scuseria, G. E.; Constantin, L. A.; Zhou, X.; Burke, K. Restoring the Density-Gradient Expansion for Exchange in Solids and Surfaces. *Phys. Rev. Lett.* **2008**, *100* (16), 039902.

(28) Grimme, S. Semiempirical GGA-Type Density Functional Constructed with a Long-Range Dispersion Correction. *J. Comput. Chem.* **2006**, *27*, 1787–1799.

(29) Adamo, C.; Barone, V. Toward Reliable Density Functional Methods without Adjustable Parameters: The PBE0Model. *J. Chem. Phys.* **1999**, *110* (13), 6158–6170.

(30) Even, J.; Pedesseau, L.; Jancu, J.-M.; Katan, C. Importance of Spin–Orbit Coupling in Hybrid Organic/Inorganic Perovskites for

Photovoltaic Applications. *J. Phys. Chem. Lett.* **2013**, *4* (17), 2999–3005.

(31) Wiktor, J.; Rothlisberger, U.; Pasquarello, A. Predictive Determination of Band Gaps of Inorganic Halide Perovskites. *J. Phys. Chem. Lett.* **2017**, *8*, 5507–5512.

(32) Macrae, C. F.; Bruno, I. J.; Chisholm, J. A.; Edgington, P. R.; McCabe, P.; Pidcock, E.; Rodriguez-Monge, L.; Taylor, R.; Streek, J. v.; Wood, P. A. Mercury CSD 2.0—New Features for the Visualization and Investigation of Crystal Structures. *J. Appl. Crystallogr.* **2008**, *41*, 466–470.